

1 **Role of heterogeneous surface wettability on dynamic immiscible**
2 **displacement, capillary pressure, and relative permeability in a CO₂-**
3 **water-rock system**

4 Ruichang Guo^a, Laura Dalton^b, Dustin Crandall^c, James McClure^d, Hongsheng Wang^a, Zhe Li^e,
5 Cheng Chen^f

6 ^a Department of Mining and Minerals Engineering, Virginia Tech, Blacksburg, VA

7 ^b Department of Civil, Construction, and Environmental Engineering, North Carolina State
8 University, Raleigh, NC

9 ^c U.S. Department of Energy National Energy Technology Laboratory, Morgantown WV

10 ^d Advanced Research Computing, Virginia Tech, Blacksburg, VA

11 ^e Department of Electronic Materials Engineering, Research School of Physics, The Australian
12 National University

13 ^f Department of Civil, Environmental and Ocean Engineering, Stevens Institute of Technology,
14 Hoboken, NJ

15 **Abstract:** Surface wettability is one of the major factors that regulate immiscible fluid
16 displacement in porous media. However, the role of pore-scale wettability heterogeneity on
17 dynamic immiscible displacement is rarely investigated. This study investigated the impact of
18 pore-scale wettability heterogeneity on immiscible two-fluid displacement and the resulting
19 macroscopic constitutive relations, including the capillary pressure-water saturation (P_c - S_w) and
20 relative permeability curves. A digital Bentheimer sandstone model was obtained from X-ray
21 micro-computed tomography (micro-CT) scanning and the rock surface wettability fields were
22 generated based on in-situ measurements of contact angles. A graphics processing unit-accelerated
23 lattice Boltzmann model was employed to simulate the immiscible displacement processes through
24 the primary drainage, imbibition, and second drainage stages in a CO₂-water-rock system. We
25 found that pore-scale surface wettability heterogeneity caused noticeable local supercritical CO₂
26 (scCO₂) and water redistribution under less water-wet conditions. At the continuum scale, the P_c -
27 S_w curves under the heterogeneous wetting condition were overall similar to those under the
28 homogeneous wetting condition. This is because the impact of local wettability heterogeneity on
29 the large-scale capillary pressure-water saturation curve was statistically averaged out at the entire-
30 sample scale. The only difference was that heterogeneous wettability led to a negative entry
31 pressure at the primary drainage stage under the intermediate-wet condition, which was caused by

32 local, scCO₂-wet surfaces. The impact of pore-scale wettability heterogeneity was more noticeable
33 on the relative permeability curves. Particularly, the variation of the scCO₂ relative permeability
34 curve in the heterogeneous wettability scenario was more significant than that in the homogenous
35 wettability scenario. This suggests that pore-scale wettability heterogeneity enhances the
36 coalescence and snap-off behaviors of scCO₂ blobs. This is the first study that systematically
37 investigated the role of pore-scale contact angle heterogeneity on dynamic immiscible
38 displacement and associated P_c-S_w curves in complicated, three-dimensional porous media.

39 **Key words:** geological CO₂ sequestration, immiscible displacement, wettability heterogeneity,
40 P_c-S_w curve, relative permeability

41 Correspondence to: C. Chen: cchen6@stevens.edu

42

43 1. Introduction

44 Mitigation of the global climate change has become an urgent and pressing challenge of our time.
45 The 2015 Paris Agreement aimed to keep the global average temperature increase within 2 °C
46 compared to pre-industrial period and to achieve net-zero emissions ultimately (IPCC,
47 2018; Hassanpouryouzband et al., 2021). Geological carbon sequestration (GCS) has proven a
48 viable solution to mitigating CO₂ emissions while allowing continued large-scale consumptions of
49 fossil fuel energy (Michael et al., 2010; Tang et al., 2019). Subsurface saline aquifers have been
50 considered ideal geological formations for GCS due to their extensive distribution and vast storage
51 capacity, which was estimated to be 320 – 10,000 gigatons of CO₂ across the world (Bachu, 2002).
52 After the emplacement of CO₂ in a deep saline aquifer, the CO₂ exists in the supercritical phase if
53 the temperature is higher than 31 °C and pressure is higher than 1,000 psi (Chen et al., 2013). The
54 supercritical CO₂ (scCO₂) migrates upward due to buoyancy and then spreads horizontally when
55 it reaches the impermeable cap rock (Sathaye et al., 2014; Emami-Meybodi et al., 2015; Guo et al.,
56 2021). It is critical to understand and predict the migration of scCO₂ in saline aquifers to ensure
57 the long-term security of GCS (Chang et al., 2020).

58 The migration of injected scCO₂ in saline aquifers can be modeled as an immiscible displacement
59 process, which is regulated by the pore geometry, fluid properties, and rock surface wettability
60 (Tanino and Blunt, 2013). The surface wettability of a porous medium is usually characterized as
61 the static contact angle (CA), the distribution of which on rock surfaces can be homogeneous or
62 heterogeneous. In general, water is referred to as the wetting-phase fluid because its CA is usually
63 smaller than 90 degrees, whereas another fluid (e.g., scCO₂ or oil) is referred to as the nonwetting-

64 phase fluid (Fan et al., 2019). The impact of homogeneous wettability on multiphase flow in porous
65 media has been intensively studied (Pan et al., 2004;Li et al., 2005;Boek et al., 2017;Leclaire et
66 al., 2017;Tang et al., 2019;Bakhshian et al., 2021). However, studies on rock samples strongly
67 suggested that the surface wettability in a natural rock is heterogeneous (Morrow, 1975;Bradford
68 and Leij, 1995;Hwang et al., 2006;Rucker et al., 2019;Arshadi et al., 2020;Guo et al., 2020).
69 Previous studies usually modeled heterogeneous surface wettability as a mixture of two types of
70 surfaces, with one being water-wet and the other being oil-wet. The heterogeneous surface
71 wettability model can be further classified as fractional wettability and mixed wettability,
72 depending on whether the distribution of surface wettability is a function of pore size. A fractional
73 wettability model assumes that the distribution of wetting surfaces is independent of the pore size,
74 whereas a mixed wettability model assumes that rock surfaces in small pores are water-wet and
75 rock surfaces in large pores are oil-wet (Valvatne and Blunt, 2004;Skauge et al., 2007). The overall
76 wettability of a porous medium is usually modified by changing the ratio between the wetting and
77 non-wetting surfaces for a fractional wettability model and the extent of surface property alteration
78 for a mixed wettability model (Zhao et al., 2018;Chang et al., 2020).

79 Recently published studies on in-situ measurements of surface wettability suggested that the
80 surface wettability of a natural rock can cover a wide range of CAs rather than only two CAs
81 (Saraji et al., 2013;Andrew et al., 2014;Alhammadi et al., 2017;Mutailipu et al., 2017;AIRatrou
82 et al., 2018;Arshadi et al., 2020;Guo et al., 2020;Liu et al., 2020). Our previous work (Guo et al.,
83 2020) modeled the heterogeneous surface wettability in a sandstone sample as a Gaussian random
84 field with a spatial correlation length based on in-situ CA measurements using X-ray micro-
85 computed tomography (micro-CT). To adequately leverage the power of pore-scale numerical
86 simulation of multiphase flow in porous media, it is critical to accurately describe and incorporate
87 the detailed surface wettability information into the model (Akai et al., 2019).

88 Constitutive relations, such as the capillary pressure-water saturation (P_c-S_w) relationship and
89 relative permeability, are critical inputs for continuum-scale simulations of multiphase flow in
90 porous media. The role of pore-scale wettability heterogeneity on the macroscopic constitutive
91 relations has attracted significant attention. Previous studies have intensively investigated the
92 displacement mechanisms under different wetting conditions (Zhao et al., 2016;Hu et al., 2017)
93 and the effect of surface wettability on capillary pressure and relative permeability (Hwang et al.,
94 2006;Landry et al., 2014;Zhao et al., 2018;Bakhshian and Hosseini, 2019;Chang et al.,
95 2020;Nemer et al., 2020). In the studies on fractional wettability, the physical model for fractional-
96 wet porous media were constructed by mixing sands having different wettability (Bradford and
97 Leij, 1995;Hwang et al., 2006), mixing beads having designed wettability (Murison et al.,
98 2014;Hiller et al., 2019), and mapping surface wettability fields to digital rock models (Bakhshian

99 and Hosseini, 2019). It was observed that an increasing fraction of non-wetting surface led to
100 increasing wetting-phase relative permeability and decreasing non-wetting-phase relative
101 permeability (Bradford and Leij, 1995;Hwang et al., 2006). However, the impact of fractional
102 wettability on capillary pressure is more complicated. In an oil-water or CO₂-water system, it was
103 observed that increased fraction of non-wetting sand reduces the capillary pressure in both the
104 primary drainage and imbibition curves (Bradford and Leij, 1995;Hwang et al., 2006). In an air-
105 water system, Hwang’s results showed that there was no noticeable relationship between the
106 fraction of non-wetting surface and capillary pressure (Hwang et al., 2006). Studies using beads
107 with designed wettability patterns showed that the spatial correlation length also had an impact on
108 capillary pressure; particularly, a smaller spatial correlation length enhanced the hysteresis in the
109 *P_c-S_w* curves (Murison et al., 2014;Hiller et al., 2019).

110 A mixed wettability model assumes that the oil-wet surfaces were caused by the contact with oil.
111 Mixed-wet porous media were typically constructed using the surface aging method, which altered
112 water-wet surfaces using non-wetting fluids (Masalmeh, 2002;Tanino and Blunt, 2013;Chang et
113 al., 2020;Qin et al., 2020). The impact of mixed wettability on relative permeability varied, which
114 depended on the extent of surface property alteration. It was observed that mixed wettability
115 decreased oil relative permeability and increased water relative permeability (Zou and Armstrong,
116 2019;Nemer et al., 2020). The influence of mixed wettability on oil relative permeability was more
117 significant than on water relative permeability. The impact on water relative permeability was
118 small and sometimes negligible (Landry et al., 2014). In the imbibition stage under the mixed-wet
119 condition, a non-monotonic relation between the initial oil saturation and remaining oil saturation
120 was observed (Tanino and Blunt, 2013). Mixed wettability can also cause preferential non-wetting
121 flow paths (Chang et al., 2020).

122 In the laboratory, it is challenging to construct a rock sample having desired heterogeneous surface
123 wettability and to investigate displacement dynamics at the pore scale. Therefore, pore-scale
124 simulation, such as the lattice Boltzmann (LB) method, has become a powerful tool to unravel the
125 role of pore-scale wettability heterogeneity on large-scale displacement dynamics (Berg et al.,
126 2013;Andrew et al., 2015;Nemer et al., 2020). The LB method also has advantages in incorporating
127 complex physicochemical properties, such as surface wettability, solubility, and phase separation,
128 compared to traditional computational fluid dynamics models (Shi and Tang, 2018;Zhao et al.,
129 2018;Guo et al., 2020;McClure et al., 2021). In addition, the rapid development of graphics
130 processing unit (GPU)-based parallel computing technologies makes the LB method an efficient
131 numerical scheme in simulating large-scale multiphase flow in porous media (McClure et al.,
132 2010;McClure et al., 2014;Xue and Roy, 2021).

133 Although many studies have been conducted to investigate immiscible two-fluid displacements in
134 porous media, there is still a lack of fundamental understanding of immiscible displacements under
135 heterogeneous wettability conditions. This study investigated the impact of pore-scale surface
136 wettability heterogeneity, which has a wide range of CA distribution, on the dynamic immiscible
137 displacement process in a Bentheimer sandstone. The heterogeneous wettability fields were
138 generated based on the CA variance and spatial correlation length measured from X-ray micro-CT
139 images of a Bentheimer sandstone, which were then imported into a LB multiphase flow model as
140 rock surface properties. Compared to one of our recent publications (Guo et al., 2020), which
141 focused on steady-state two-phase flow in porous media, this work focuses on transient,
142 immiscible two-fluid displacement in porous media. Particularly, the goal of this study is to
143 investigate the role of pore-scale surface wettability heterogeneity on large-scale immiscible
144 displacement dynamics and the associated Pc - Sw curves, which has extensive applications in many
145 geo-energy and hydrogeological systems associated with multiphase flow in complicated porous
146 media (Chen and Ewing, 1997;Hewitt, 2008;Feng et al., 2021;Li et al., 2022).

147

148 **2. Materials and Methods**

149 **2.1. LB method for multiphase flow modeling**

150 The color-gradient LB multiphase flow model was used in this study for numerical simulation of
151 immiscible two-phase displacement in the sandstone and calculations of the Pc - Sw curves and
152 relative permeability. The LB method has proven an efficient tool to simulating multiphase flow
153 in complex 3D porous media (McClure et al., 2014;Guo et al., 2020), and the LB model used in
154 this study has been validated and published in our previous studies (Fan et al., 2019;Fan et al.,
155 2020;Guo et al., 2020). In our LB model, the momentum equation is simulated using the D3Q19
156 lattice structure, which means there are 19 velocity directions in the 3D space. The discrete velocity
157 vectors in D3Q19 are:

$$\begin{cases} (0, 0, 0) & \text{for } q = 0 \\ (\pm 1, 0, 0) & \text{for } q = 1, 2 \\ (0, \pm 1, 0) & \text{for } q = 3, 4 \\ (0, 0, \pm 1) & \text{for } q = 5, 6 \\ (\pm 1, \pm 1, 0) & \text{for } q = 7, 8, 9, 10 \\ (\pm 1, 0, \pm 1) & \text{for } q = 11, 12, 13, 14 \\ (0, \pm 1, \pm 1) & \text{for } q = 15, 16, 17, 18 \end{cases} \quad (1)$$

159 In order to reduce the computing costs, the mass transfer equation was simulated using a D3Q7
160 lattice structure (McClure et al., 2014). The corresponding velocity vectors in D3Q7 are the first

161 seven vectors in Equation 1. The mass distributions for the wetting fluid and non-wetting fluid are
 162 constructed using their densities, ρ^w and ρ^n , and the velocity, \mathbf{u} :

$$163 \quad \begin{aligned} g_q^w &= w_q \left[\rho^w (1 + \mathbf{e}_q \cdot \mathbf{u}) + \beta (\mathbf{e}_q \cdot \mathbf{n}) \rho^n \rho^w / (\rho^n + \rho^w) \right] & q = 0, 1, 2, \dots, 6 \\ g_q^n &= w_q \left[\rho^n (1 + \mathbf{e}_q \cdot \mathbf{u}) - \beta (\mathbf{e}_q \cdot \mathbf{n}) \rho^n \rho^w / (\rho^n + \rho^w) \right] & q = 0, 1, 2, \dots, 6 \end{aligned} \quad (2)$$

164 where weights w_q are 1/3 for $q = 0$ and 1/9 for $q = 1, 2, \dots, 6$, and \mathbf{n} is the unit vector normal to
 165 the fluid-fluid interface. The superscripts w and n refer to the wetting fluid and nonwetting fluid,
 166 respectively.

167 The fluid densities are then calculated as:

$$168 \quad \rho^i(\mathbf{x}, t + \Delta t) = \sum_{q=0}^6 g_q^i(\mathbf{x} - \mathbf{e}_q \Delta t, t) \quad i = w, n \quad (3)$$

169 In the multi-relaxation-time approach, the collision process is simulated in the moment space. The
 170 transformation between moments, \mathbf{m} , and the distribution function, \mathbf{f} , are written as:

$$171 \quad \mathbf{m} = M \cdot \mathbf{f}, \quad \mathbf{f} = M^{-1} \cdot \mathbf{m} \quad (4)$$

172 where M is the transformation matrix, and M^{-1} is the inverse of M .

173 The particle distribution evolution equation is written as:

$$174 \quad f_q(\mathbf{x} + \mathbf{e}_q \Delta t, t + \Delta t) - f_q(\mathbf{x}, t) = \sum_{i=0}^{Q-1} M_{qi}^{-1} \Lambda_i (m_i^{eq} - m_i) \quad q = 0, 1, 2, \dots, 18 \quad (5)$$

175 where $f_q(\mathbf{x}, t)$ is the particle distribution function at location \mathbf{x} and time t travelling in the q^{th}
 176 direction; $f_q(\mathbf{x} + \mathbf{e}_q \Delta t, t + \Delta t)$ is the particle distribution function at the adjacent lattice node after
 177 each streaming step in the q^{th} direction; Λ_i is the i^{th} relaxation rate of moment m_i toward its
 178 corresponding equilibrium value, m_i^{eq} .

179 To simulate the interfacial tension, additional terms are incorporated into the non-zero equilibrium
 180 moments:

181

$$\begin{aligned}
m_1^{eq} &= (j_x^2 + j_y^2 + j_z^2) + \alpha |\mathbf{C}| \\
m_9^{eq} &= (2j_x^2 - j_y^2 - j_z^2) + \alpha \frac{|\mathbf{C}|}{2} (2n_x^2 - n_y^2 - n_z^2) \\
m_{11}^{eq} &= (j_y^2 - j_z^2) + \alpha \frac{|\mathbf{C}|}{2} (n_y^2 - n_z^2) \\
m_{13}^{eq} &= j_x j_y + \alpha \frac{|\mathbf{C}|}{2} n_x n_y \\
m_{14}^{eq} &= j_y j_z + \alpha \frac{|\mathbf{C}|}{2} n_y n_z \\
m_{15}^{eq} &= j_x j_z + \alpha \frac{|\mathbf{C}|}{2} n_x n_z
\end{aligned} \tag{6}$$

182

183

184

where j_x , j_y , and j_z are fluid momentums in the x, y, and z directions, respectively; α is the parameter to adjust the interfacial tension; \mathbf{C} is the color gradient; n_x , n_y , and n_z are the components of the unit norm vector, \mathbf{n} , in the x, y, and z directions, respectively.

185

186

187

188

189

190

191

192

193

194

195

196

197

198

199

200

201

202

203

204

205

206

207

208

In the LB simulation of immiscible two-fluid displacement, a buffer layer with a thickness of six lattice units (lus) was placed at both ends of the rock in the main flow direction. The buffer layer at the inlet was set as scCO₂ whereas the buffer layer at the outlet was set as water. The kinematic viscosity of scCO₂ is 0.1-0.25 of water. Therefore, in this work the viscosity ratio of water to scCO₂ was set as 4:1 (Fan et al., 2019). The pressure boundary condition was applied at the inlet and outlet, and the no-slip boundary condition was applied at rock surfaces. In this work, the coefficient, α , in Equation 6 was set as 0.005. We matched the capillary number (Ca) between the LB model system and the real system to recover the correct ratio of viscous force to interfacial force. Because the Ca number was low, which indicates that the flow velocity is slow and the interfacial tension dominates over the viscous force, the impact of density ratio was negligible. Therefore, in this study the density ratio between scCO₂ and water was set as one. The rock was initially saturated with water. We gradually changed the pressure difference between the two ends of the rock sample to let the system go through the primary drainage (PD), imbibition (IM), and secondary drainage (SD) stages. The capillary pressure (i.e., pressure difference between the non-wetting fluid and wetting fluid) and water saturation in the sample were recorded when the flow reached a steady state at each pressure difference. At each water saturation, scCO₂ and water distribution in the three-dimensional (3D) pore space was extracted and then used as the initial condition to simulate the steady-state relative permeability curves. In the simulation of relative permeability, fluid flow was driven by applying a constant external body force with a periodic boundary condition in the main flow direction, which aimed to maintain a constant water saturation in the domain and to mimic fractional flow experiments typically used to measure relative permeability in the laboratory (Fan et al., 2019). To address the high demand of computing costs associated with the LB method, a hybrid, multicore central processing unit (CPU)/GPU parallel computing acceleration algorithm was employed in the implementation of the LB modeling (McClure et al., 2014; Chen et al., 2016).

209

210 **2.2. Generation of heterogeneous surface wettability**

211 The wettability of a rock surface can be characterized using the static CA measured on the
 212 sandstone surface. In our previous study (Guo et al., 2020), we conducted in-situ measurements of
 213 static CAs on the rock surfaces in a Bentheimer sandstone based on high-resolution X-ray micro-
 214 CT scanning (Wang et al., 2022). The measurements showed that the surface CA distribution
 215 follows a lognormal distribution and can be modeled as a Gaussian random field with a spatial
 216 correlation length. The log wettability field, \mathbf{Y} , is defined as $\mathbf{Y} = \log(\boldsymbol{\theta})$, where $\boldsymbol{\theta}$ is the CA random
 217 field. The mean and variance of $\boldsymbol{\theta}$ are related to the mean and variance of \mathbf{Y} by $\mu_{\theta} = e^{\mu_Y + \sigma_Y^2/2}$ and
 218 $\sigma_{\theta}^2 = (e^{\sigma_Y^2} - 1) \cdot e^{2\mu_Y + \sigma_Y^2}$, respectively (Chen and Zeng, 2015). The correlation function of the log wettability
 219 field between points \mathbf{x} and \mathbf{y} in the 3D space, $c_Y(\mathbf{x}, \mathbf{y})$, is calculated as
 220 $c_Y(\mathbf{x}, \mathbf{y}) = \sigma_Y^2 \exp[-(|x_1 - y_1|/L_1 + |x_2 - y_2|/L_2 + |x_3 - y_3|/L_3)]$, where L_1, L_2 , and L_3 are the correlation lengths in the
 221 three principal directions (Guo et al., 2020).

222 We used the Karhunen-Loève expansion (KLE) method to efficiently generate the heterogeneous
 223 wettability field on rock surfaces, which reduces the time and computer memories required
 224 compared to other methods that directly generate 3D random fields (Zhang and Lu, 2004). In the
 225 KLE method, the correlation function of the log wettability field, $c_Y(\mathbf{x}, \mathbf{y})$, is decomposed in the
 226 form of eigenvalues and eigenfunctions:

227

$$c_Y(\mathbf{x}, \mathbf{y}) = \sum_{n=1}^{\infty} \lambda_n \psi_n(\mathbf{x}) \psi_n(\mathbf{y}) \quad (7)$$

228 where λ_n and $\psi_n(\mathbf{x})$ are the n^{th} eigenvalue and eigenfunction, respectively.

229 The wettability fields are then generated using the KLE method:

230

$$\mathbf{Y}(\mathbf{x}) = \langle \mathbf{Y}(\mathbf{x}) \rangle + \sum_{n=1}^{\infty} \xi_n \sqrt{\lambda_n} \psi_n(\mathbf{x}) \quad (8)$$

231 where ξ_n are independent zero-mean Gaussian random variables having a unit variance. In
 232 practice, finite terms in the KLE method are employed to approximate the desired random fields
 233 (Chen et al., 2013). The details of this method were given in (Zhang and Lu, 2004; Guo et al., 2020).
 234 In the next step, the surface wettability of the sandstone is constructed by mapping the generated
 235 wettability field onto the surface of the Bentheimer sandstone.

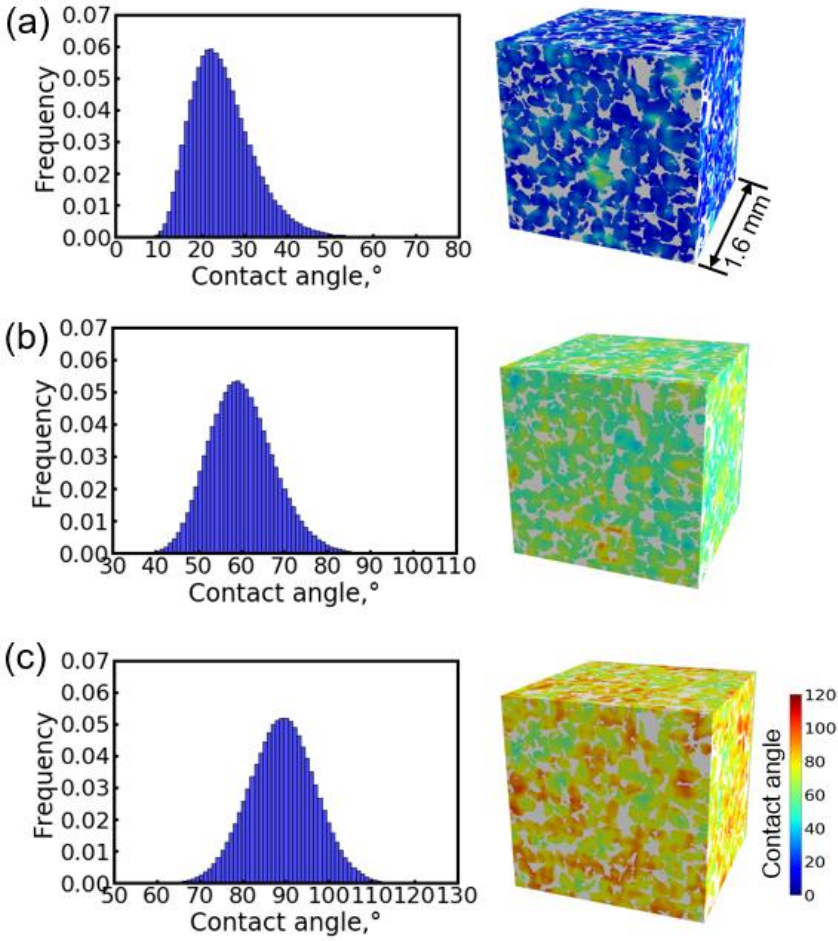
236

237 **2.3. Rock models with heterogeneous surface wettability**

238 The 3D digital rock model in this study has dimensions of $240 \times 240 \times 240$ voxels, with a micro-
239 CT resolution of $6.67 \mu\text{m}$ per pixel length. The porosity of the rock is 26%. Iglauer et al. (2015)
240 classified the rock surface wettability in a CO_2 -water-rock system into 7 types based on the value
241 of the static surface CA: completely water-wet (i.e., a CA of 0°), strongly water-wet (0° - 50°),
242 weakly water-wet (50° - 70°), intermediate wet (70° - 110°), weakly CO_2 -wet (110° - 130°), strongly
243 CO_2 -wet (130° - 180°), and completely CO_2 -wet (180°). In this study, we used this classification to
244 characterize the wetting conditions of rocks. In a saline aquifer, the sandstone is usually water-wet
245 or intermediate wet. Therefore, we only generated heterogeneous strongly water-wet (SWW),
246 weakly water-wet (WWW), and intermediate wet (IW) fields having mean CAs of 25° , 60° , and
247 90° , respectively. The standard deviation and spatial correlation length of the CA distributions
248 were 9° , and $118.6 \mu\text{m}$, respectively, which were measured in the Beithemer sandstone core after
249 two drainage-imbibition cycles of core flooding experiments using in-situ X-ray micro-CT (Guo
250 et al., 2020). Note that the dimension of the computational domain (240 pixel lengths) was 13.5
251 times larger than the spatial correlation length (17.8 pixel lengths), which suggests that sufficient
252 statistical information was included in the generated Gaussian random fields and thereby the
253 ergodicity requirement was satisfied. The generated heterogeneous wettability fields were then
254 projected onto the rock surfaces on the Bentheimer rock, as shown in **Fig. 1**. We then conducted
255 LB multiphase flow modeling in all of the three rock models to simulate the immiscible two-phase
256 displacement processes that included the PD, IM, and SD stages.

257

258



259

Fig. 1. CA distributions of generated heterogeneous wettability fields and corresponding rock models under A) SWW, B) WWW, and C) IW conditions. In the rock models, the pore space is white, and the solid is rendered with a color bar ranging from blue (water-wet) to red (CO₂-wet) that represents the range of CA values.

262

2.4. Corey model for fitting relative permeability curves

265

The Corey model was used to fit the LB-simulated water and scCO₂ relative permeabilities, which assumes that the relationship between relative permeabilities and normalized water saturations follows a power law:

268

$$k_{rw} = k_{rw}^o S_w^{*N_w} \quad (9)$$

269

$$k_{rg} = k_{rg}^o (1 - S_w^*)^{N_g} \quad (10)$$

270

271

where k_{rw} and k_{rw}^o are water relative permeability and end-point water relative permeability, respectively; k_{rg} and k_{rg}^o are scCO₂ relative permeability and end-point scCO₂ relative

272 permeability, respectively; N_w and N_g are the power-law exponents for water and scCO₂ relative
273 permeability curves, respectively. S_w^* is the normalized water saturation defined as
274 $S_w^* = (S_w - S_{wir}) / (1 - S_{wir} - S_{grw})$, where S_w is water saturation, S_{wir} is irreducible water saturation,
275 and S_{grw} is residual scCO₂ saturation.

276

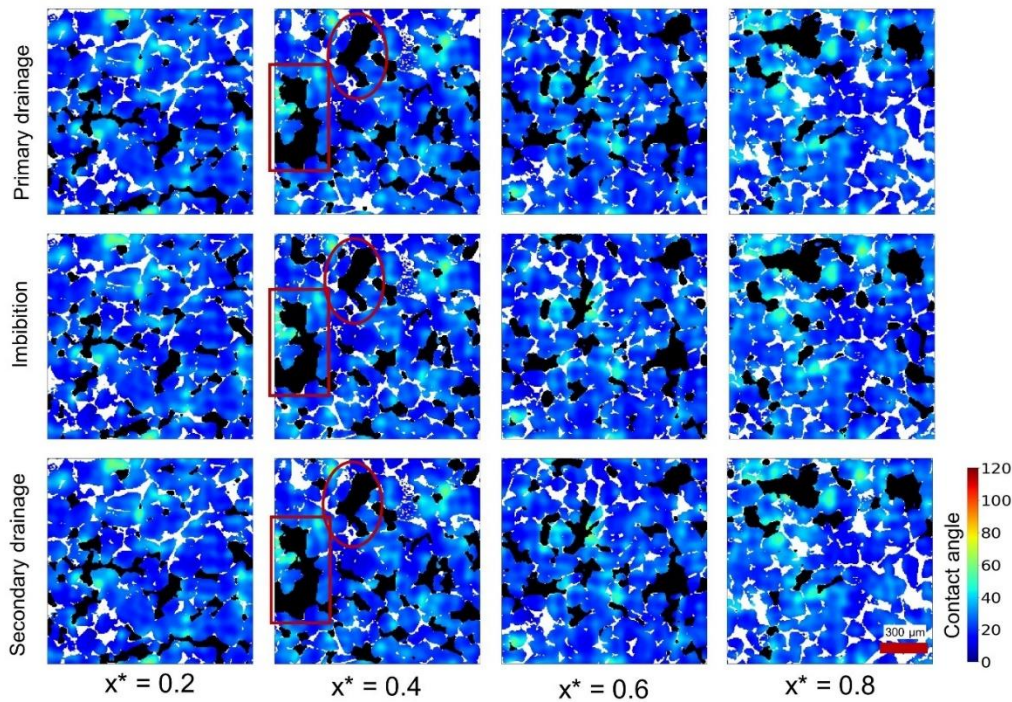
277 **3. Results and discussion**

278 **3.1. Pore-scale scCO₂ and water distribution**

279 The pore geometry, rock surface wettability, and saturation history determine the scCO₂ and water
280 distribution at the pore scale. Wettability is the competition between scCO₂ and water to adhere to
281 rock surfaces (Nemer et al., 2020). Pore-scale heterogeneity of rock surface wettability can cause
282 redistribution of scCO₂ and water in the pore space. **Figs. 2-4** demonstrate pore-scale scCO₂ and
283 water distribution under different wetting conditions in the PD, IM, and SD stages. To better
284 demonstrate the surface wettability heterogeneity, pore-scale surface wettability distributions were
285 illustrated in Figs. 2-4 using the color bars that indicated the distribution of surface CAs.

286 Under the SWW and WWW conditions, the shape and distribution of scCO₂ blobs were
287 determined primarily by the pore geometry. The scCO₂ blobs were more likely to reside on the
288 less water-wet surfaces. We extracted pore-scale distribution maps of scCO₂ and water during the
289 transient displacement process in the PI, IM, and SD stages, as shown in Fig. 2. It can be observed
290 that the distribution of scCO₂ under the SWW condition in the PD, IM, and SD stages was almost
291 identical. In the SWW heterogeneous wettability scenario, all CAs were less than 90° with an
292 average CA of 25°. This indicated that in this scenario the scCO₂ always had lower affinity to rock
293 surfaces compared to water. Therefore, scCO₂ blobs had lower mobility because they were trapped
294 in relatively large pores due to the capillary pressure barrier, leading to similar pore-scale fluid
295 distribution maps among the PD, IM, and SD stages, as shown in Figure 2.

296



297

298

299

300

301

302

303

304

305

306

307

308

309

310

311

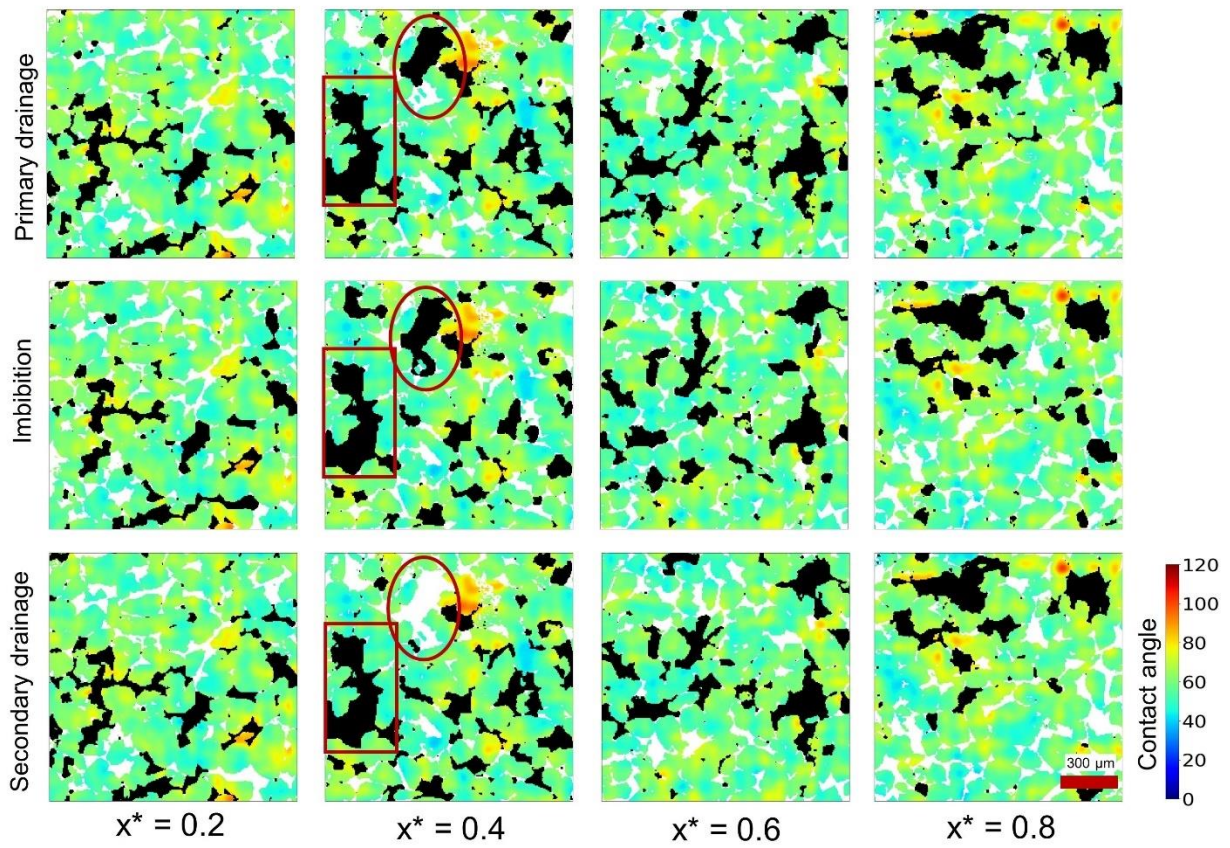
312

313

Fig. 2. Snapshots of pore-scale scCO₂ and water distribution at various dimensionless distances, x^* , under the SWW condition with a water saturation of 0.5 during the PD, IM, and SD stages. The scCO₂ is marked in black and water is marked in white. The Bentheimer sandstone is demonstrated with a color bar ranging from blue to red which indicate the distribution of surface CA values. The red ellipse and rectangle mark the scCO₂ distributions in intermediate and large pores, respectively.

Fig. 3 demonstrates the distribution of scCO₂ under the WWW condition with an average CA of 60°. Larger CAs led to lower affinity of water to rock surfaces compared to the SWW condition, which resulted in enhanced CO₂ mobility. This was confirmed by the noticeable CO₂ saturation changes in intermediate- and large-sized pores among the PD, IM, and SD stages, which suggested that the scCO₂ blobs were able to move through small pore throats and thus were not trapped in intermediate- and large-sized pores. This was further confirmed by **Fig. 4**, where rock surfaces were under the IW condition. It was noticeable that in this scenario the scCO₂ saturation variations in intermediate- and large-sized pores were significant, which suggested that the rock surfaces were neutral-wet, leading to reduced capillary pressure barriers and consequently enhanced mobility for both fluids.

314

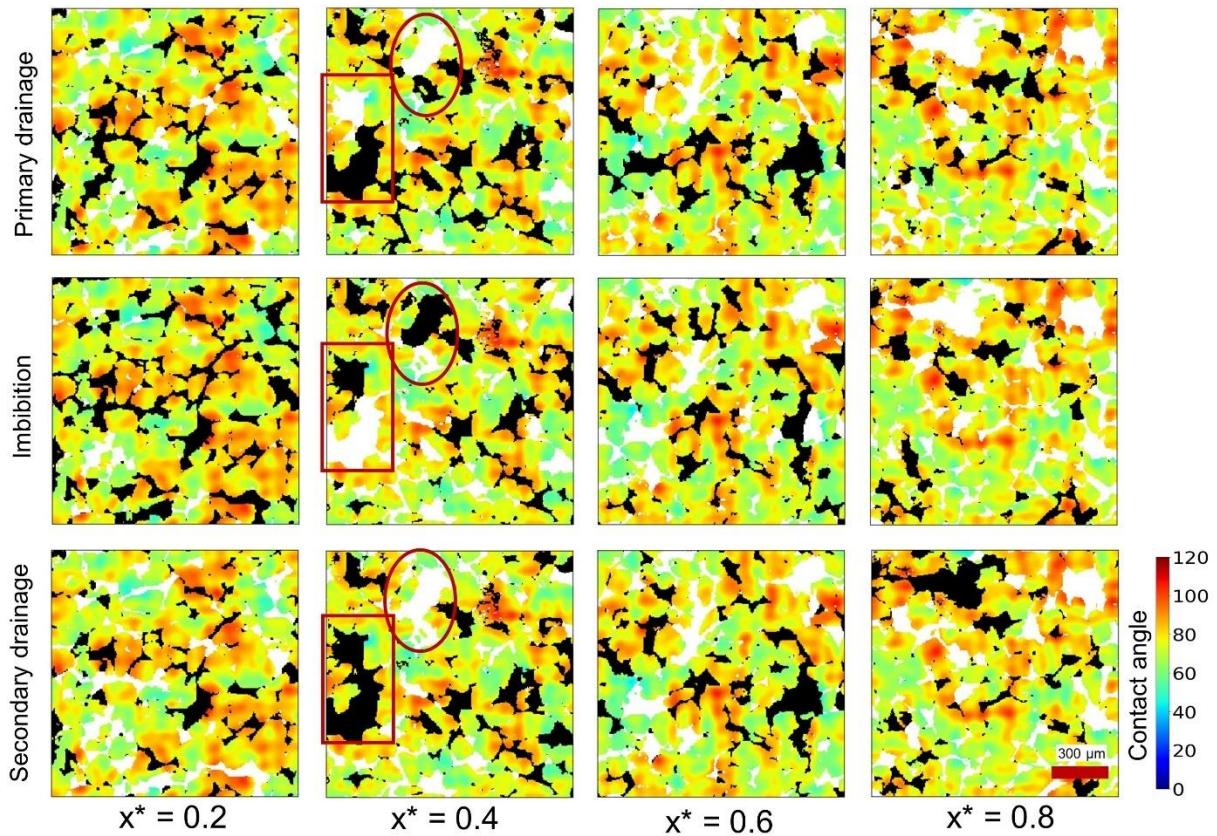


315

316

317

Fig. 3. Snapshots of pore-scale scCO_2 and water distribution at various dimensionless distances under the WWC condition with a water saturation of 0.5 during the PD, IM, and SD stages.



318

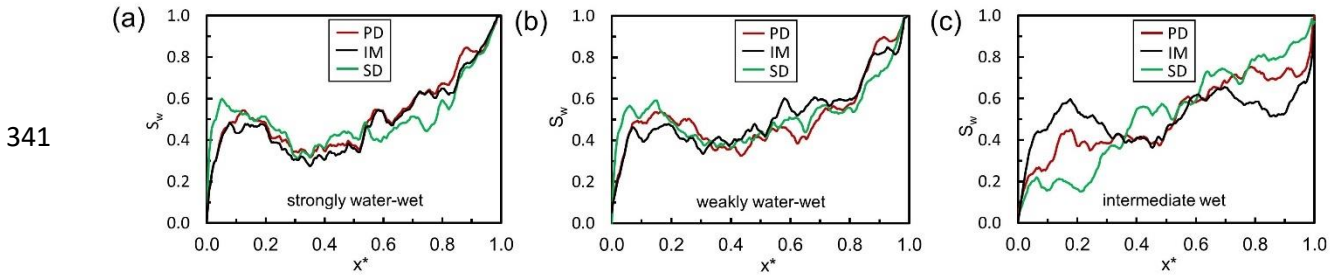
319 Fig. 4. Snapshots of pore-scale scCO₂ and water distribution at various dimensionless distances under the
 320 IW condition with a water saturation of 0.5 during the PD, IM, and SD stages.

321

322 Slice-averaged water saturation against the dimensionless distance, x^* , were plotted to elucidate
 323 the impact of rock surface wettability on the scCO₂ distribution in the longitudinal (i.e., main flow)
 324 direction. **Fig. 5** illustrates the water saturation distributions under the SWW, WWW, and IW
 325 scenarios, and the overall water saturation was 0.5 for all these scenarios. It is noticeable that the
 326 water saturation profiles were similar between the PD, IM, and SP stages under the SWW and
 327 WWW conditions, which suggested that scCO₂, the non-wetting fluid, was trapped in large- and
 328 intermediate-sized pores under the SWW and WWW conditions due to the capillary barrier
 329 pressures in small pores and throats, leading to reduced mobility of scCO₂ and consequently small
 330 variations of local fluid saturations. Conversely, under the IW condition, the capillary barrier
 331 pressures associated with small pores and throats were mitigated due to the neutral CAs on rock
 332 surfaces, resulting in enhanced scCO₂ mobility throughout the entire sample and consequently
 333 different water saturation profiles between the PD, IM, and SD stages. This suggested that surface
 334 wettability played a more noticeable role on pore- and large-scale fluid distributions under the IW

335 condition compared to the SWW and WWW conditions. These observations were consistent with
 336 the pore-scale fluid distributions shown in Figs. 2-4. Note that during the PD, IM, and SD stages,
 337 the left end of the core (i.e., $x^*=0$) was connected to a $scCO_2$ reservoir whereas the right end (i.e.,
 338 $x^*=1$) was connected to a water reservoir, which explains why the water saturation was equal to
 339 zero at the left end and equal to one at the right end.

340



342 Fig. 5. Snapshots of water saturation profile along the main flow direction under (a) SWW condition, (b)
 343 WWW condition, and (c) IW condition. Average water saturation is 0.5 for all these water saturation
 344 profiles.

345

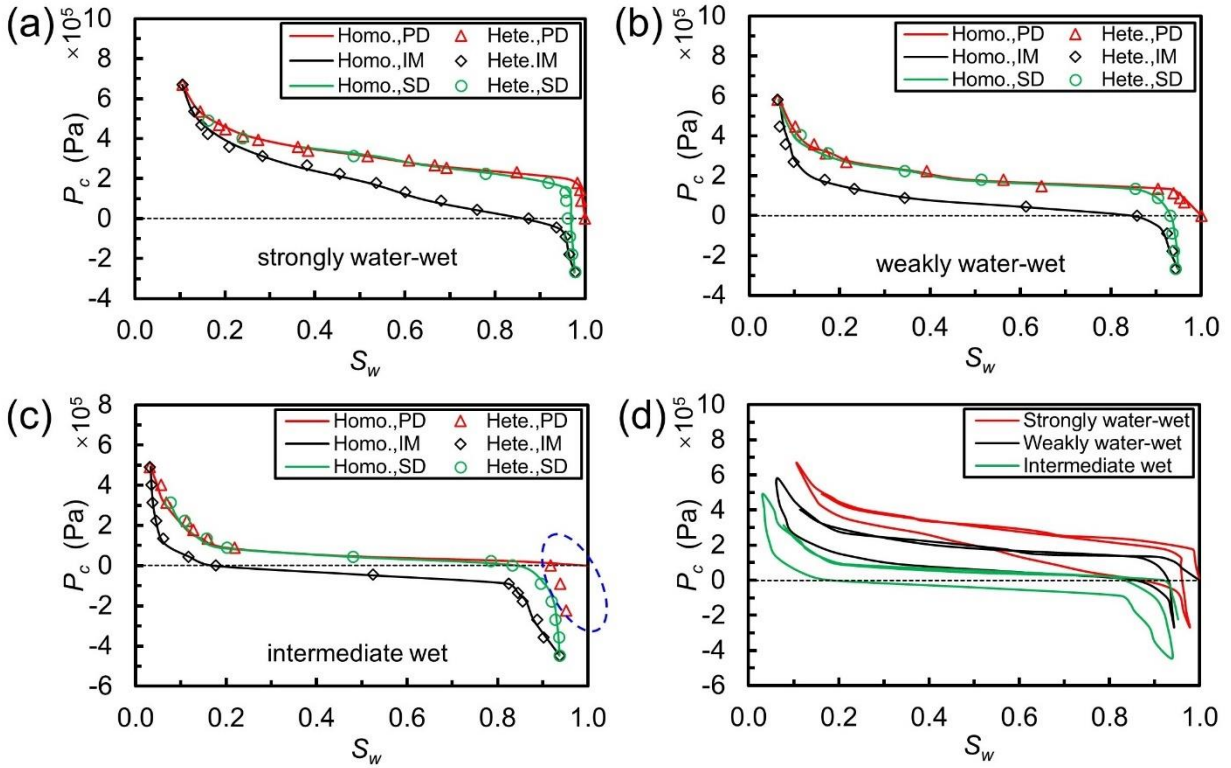
346 3.2. Capillary pressure

347 The relation between capillary pressure and water saturation, commonly characterized as the P_c -
 348 S_w curve, is a fundamental constitutive equation for predicting CO_2 migration and capillary
 349 trapping (Tokunaga et al., 2013). The factors regulating the P_c - S_w curve including pore structure,
 350 rock surface wettability, and saturation history (Bakhshian and Hosseini, 2019). In this work, the
 351 P_c - S_w curve under the SWW, WWW, and IW conditions were numerically simulated using the
 352 LB multiphase flow model. During the two-phase displacement, the pressure difference between
 353 the inlet and outlet was gradually increased or decreased, leading to a varying capillary pressure
 354 in the drainage-imbibition-drainage process. The simulation time at each pressure difference was
 355 adequately long to allow the $scCO_2$ -water-rock system to reach a steady state. Toward the end of
 356 the PD stage, when the absolute value of the first-order derivative of the P_c - S_w curve (i.e., ratio of
 357 capillary pressure change to water saturation change) was higher than a particular threshold, the
 358 drainage displacement simulation was terminated; this indicates a moment when an adequately
 359 large capillary pressure was applied but no noticeable water saturation change was observed,
 360 leading to the end point of the PD stage. Similar method was used to determine the end points of
 361 the IM and SD stages. Through these dynamic displacement processes, the Ca number ranged from
 362 10^{-7} to 10^{-3} .

363 **Fig. 6** illustrates the P_c - S_w curves for both homogeneous and heterogeneous surface wettability
364 under the SWW, WWW, and IW conditions. Under the homogeneous SWW, WWW, and IW
365 conditions, the contact angles were homogeneous over the entire rock surface and set as 25° , 60° ,
366 and 90° , respectively, which were the mean contact angles for the corresponding heterogeneous
367 wetting conditions. Fig. 6a-6c show that the P_c - S_w curves for homogeneous and heterogeneous
368 surface wettability were almost identical. This suggests although pore-scale heterogeneity induced
369 local redistribution of scCO₂ and water blobs, it had almost no effect on the large-scale P_c - S_w
370 curve which was an average property of the entire sample. In other words, the local variations of
371 scCO₂ and water distribution caused by surface wettability heterogeneity were statistically
372 averaged out at the entire-sample scale. One noticeable difference between the homogeneous and
373 heterogeneous scenarios can be found under the IW condition as shown in Fig. 6c, where the entry
374 capillary pressure of the PD section was zero for the homogeneous scenario whereas it was
375 negative for the heterogeneous scenario. This was because under the IW condition and
376 heterogeneous surface wettability a large fraction of rock surfaces had CAs larger than 90 degrees,
377 leading to local, CO₂-wet surfaces at these areas; consequently, scCO₂ can migrate into the rock
378 spontaneously, leading to a negative entry capillary pressure. In practice, a negative entry capillary
379 pressure has significant influences on field-scale CO₂ migration and distribution in a saline aquifer
380 (Singh et al., 2021).

381 Fig. 6d demonstrates the comparison of the P_c - S_w curves between the SWW, WWW, and IW
382 conditions in rock samples having heterogeneous surface wettability. When surface wettability
383 changed from SWW to IW sequentially, the P_c - S_w curves shifted in the left and downward
384 directions, leading to a lower capillary pressure at the same water saturation, a lower irreducible
385 water saturation at the end of the PD stage, and a higher residual CO₂ saturation at the end of the
386 IM stage.

387



388

389 Fig. 6. Comparison of P_c - S_w curves between homogeneous and heterogeneous wettability distributions
 390 under (a) SWW, (b) WWW, and (c) IW conditions. (d) Comparison of P_c - S_w curves under heterogeneous
 391 SWW, WWW, and IW conditions.

392

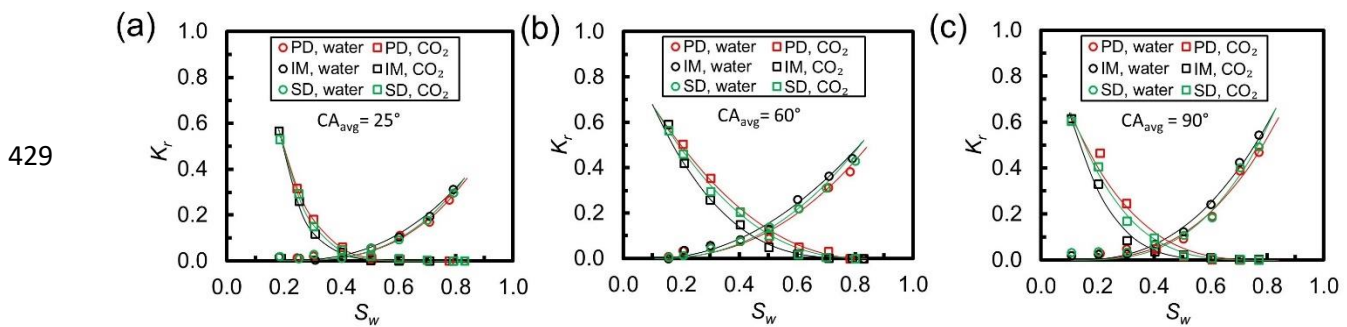
393 3.3 Relative permeability

394 The relative permeabilities under homogeneous and heterogeneous wetting conditions were also
 395 simulated. The Ca number in these simulations was 10^{-5} , which was in the range of the Ca number
 396 (between 3×10^{-9} and 3×10^{-5}) encountered in real CO_2 aquifer storage projects (Wei et al., 2014).
 397 The relatively low Ca number suggested that the interfacial force dominated the transport of the
 398 two fluids (Fan et al., 2019). **Fig. 7** illustrates the relative permeability curves under heterogeneous
 399 rock surface wettability and the SWW, WWW, and IW conditions. When the system moved from
 400 the PD stage into the IM stage, the relative permeability of scCO_2 decreased whereas the relative
 401 permeability of water increased. In other words, the relative permeability curves rotated in the
 402 counterclockwise direction. This was because in the PD stage, scCO_2 was injected into the rock,
 403 leading to enhanced connectivity of scCO_2 in the pore space, especially through small pore throats,
 404 which was favorable for the relative permeability of scCO_2 and unfavorable for the relative
 405 permeability of water. In the IM stage, water returned into the rock, leading to enhanced
 406 connectivity of water and disconnected scCO_2 blobs trapped in big pores, which enhanced the

407 relative permeability of water and decreased the relative permeability of scCO₂. Based on the same
 408 mechanism, when the system moved from the IM stage into the SD stage, the relative permeability
 409 of water decreased whereas the relative permeability of scCO₂ increased (i.e., the relative
 410 permeability curves rotated in the clockwise direction). These phenomena can be clearly observed
 411 under the IW condition (i.e., Fig 7c) because the average rock surface CA in this case was 90
 412 degrees, leading to enhanced mobility for both fluids. Conversely, under the SWW (i.e., Fig. 7a)
 413 and WWW (i.e., Fig. 7b) conditions these variations were not as noticeable as under the IW
 414 condition, because the water-wet rock surfaces limited the mobility of both fluids, which was
 415 confirmed in Figs. 2-3. These findings showed that the relative permeability can be influenced by
 416 the saturation history.

417 In addition, it was observed that in all of these wettability conditions (i.e., Figs. 7a-7c) the variation
 418 of the scCO₂ relative permeability curves between the PD, IM, and SD stages was more significant
 419 than that of the water relative permeability curves. This was because the viscosity of scCO₂ was
 420 25% of water viscosity (Chen and Zhang, 2009). During the PD and SD stages, a low-viscosity
 421 fluid (i.e., scCO₂) was forced to displace a high-viscosity fluid (i.e., water), leading to scCO₂
 422 coalescence and finger-shaped displacement fronts, thereby noticeably enhancing the connectivity
 423 and consequently the relative permeability of scCO₂. During the IM stage, scCO₂ was subject to
 424 snap-off due to its lower viscosity compared to water, leading to isolated scCO₂ blobs trapped in
 425 large pores, which significantly reduced the connectivity and consequently the relative
 426 permeability of scCO₂. Therefore, the variation of the scCO₂ relative permeability curves was more
 427 noticeable than water when the system went through the PD, IM, and SD stages.

428

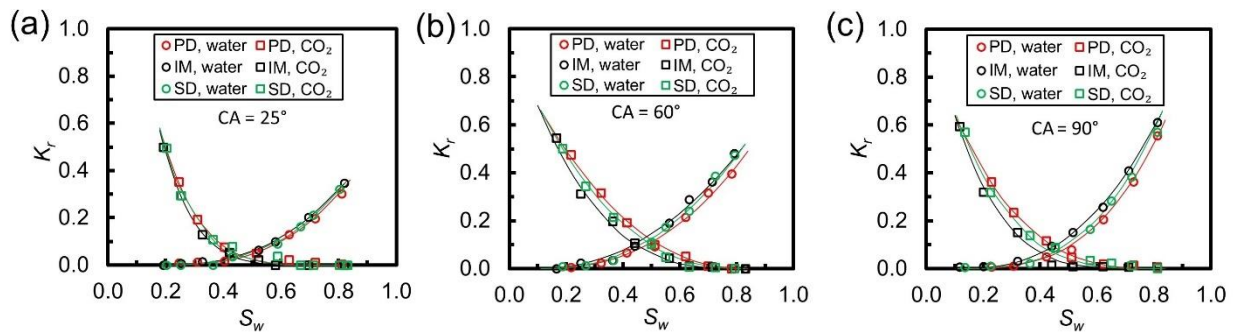


430 **Fig. 7.** Relative permeabilities for water and scCO₂ under heterogeneous (a) SWW, (b) WWW and (c) IW
 431 conditions. The scatter data points are LB-simulated relative permeabilities, whereas the solid lines are
 432 fitted relative permeability curves using the Corey model.

433

434 **Fig. 8** illustrates the relative permeability curves under homogeneous rock surface wettability and
 435 the SWW, WWW, and IW conditions. The overall evolution pattern of the relative permeability
 436 curves was similar to that in the heterogeneous wettability scenario when the system went through
 437 the PD, IM, and SD stages. However, it can be observed that the variation of the scCO₂ relative
 438 permeability curves between the PD, IM, and SD stages was less than that in the heterogeneous
 439 wettability scenario, especially under the WWW and IW conditions. This suggests that pore-scale
 440 CA heterogeneity enhances the coalescence and snap-off behaviors of scCO₂ blobs, as described
 441 before, which consequently leads to more significant variations of scCO₂ relative permeability at
 442 the larger scale.

443



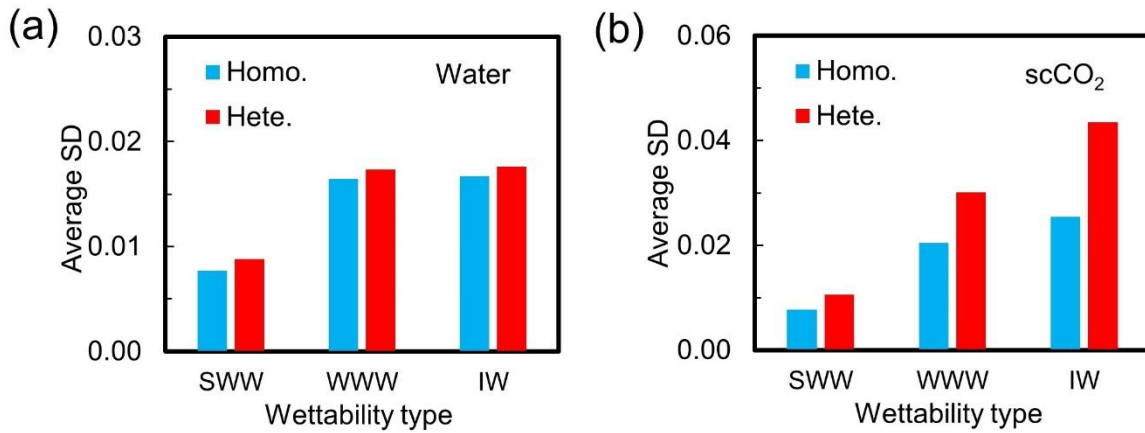
444

445 **Fig. 8.** Relative permeabilities for water and scCO₂ under homogeneous (a) SWW, (b) WWW and (c) IW
 446 conditions. The scatter data points are LB-simulated relative permeabilities, whereas the solid lines are
 447 fitted relative permeability curves using the Corey model.

448

449 To quantify the role of surface wettability heterogeneity on relative permeability, the standard
 450 deviations among the Corey-model-fitted relative permeabilities were calculated. Specifically, the
 451 relative permeabilities in the water saturation range between 0.2 and 0.8 were used. At each water
 452 saturation, the relative permeability values from the PD, IM, and SD relative permeability curves
 453 were extracted and then the standard deviation of these three values was calculated. The average
 454 standard deviation over the entire water saturation domain was calculated, which indicates the
 455 variation between the PD, IM, and SD relative permeability curves. **Fig. 9** illustrates the average
 456 standard deviations for the water and scCO₂ relative permeability curves under the three surface
 457 wettability conditions. It is clear that under the WWW and IW conditions the average standard
 458 deviations of the scCO₂ relative permeability curves between the PD, IM, and SD stages in the
 459 heterogeneous wettability scenario were noticeably higher than those in the homogeneous
 460 wettability scenario, which confirms the observations in Figs 8-9. In addition, it is clear that the
 461 average standard deviations of the scCO₂ relative permeability curves between the PD, IM, and

462 SD stages were always higher than those for water in both the homogeneous and heterogeneous
 463 wettability scenarios, which is also consistent with the observations in Figs 8-9.



464 **Fig. 9.** Average standard deviations (SDs) of relative permeability curves for water (a) and scCO₂ (b) under
 465 the SWW, WWW, and IW conditions.
 466

467
 468 **4. Summary and Conclusion**

469 Surface wettability is one of the major factors that regulate immiscible two-phase displacements
 470 in porous media. This study modeled heterogeneous surface wettability in a Bentheimer sandstone
 471 sample of which the 3D pore structure information was obtained using X-ray micro-CT scanning.
 472 The pore-scale, heterogeneous surface wettability fields were generated using Gaussian random
 473 fields based on the mean, standard deviation, and spatial correlation length obtained from in-situ
 474 measurements of CAs in the micro-CT images. The immiscible two-phase displacements were
 475 simulated using a LB multiphase flow simulator which was accelerated with a hybrid, multicore
 476 CPU/GPU parallel computing algorithm. The simulation results indicated that pore-scale
 477 heterogeneity of rock surface wettability caused noticeable redistribution of fluids at the pore scale.
 478 Previous investigations suggested that the fraction of the non-wetting fluid occupying small pores
 479 increased as the wettability switched from homogeneous SWW to homogeneous IW conditions
 480 (Bakhshian et al., 2021). This is consistent with the results in this study. Particularly, when the
 481 CO₂-water-rock system switched from the heterogeneous SWW condition to heterogeneous IW
 482 condition, scCO₂ blobs tended to reside in regions having relatively large CAs at the sub-pore
 483 scale. The wettability heterogeneity coupled with different saturation histories (i.e., PD, IM, and
 484 SD stages) enhanced the variations in pore-scale scCO₂ and water distribution, especially under
 485 the IW condition.

486 Pore-scale surface wettability heterogeneity influences the *P_c-S_w* curves, which characterize the
 487 macroscopic properties in immiscible two-phase displacements. Under the heterogeneous IW

488 condition, the entry pressure of the PD stage was negative, whereas it was zero under the
489 homogeneous IW condition. The negative entry pressure in the heterogeneous CA scenario was
490 caused by local, CO₂-wet rock surfaces, which has critical implications to large-scale geological
491 CO₂ sequestration. In other stages (i.e., IM and SD), the P_c - S_w curves were almost identical
492 between the homogeneous and heterogeneous wetting conditions. The finding suggested that the
493 local effects of surface wettability heterogeneity on the P_c - S_w curve were averaged out at the
494 entire-sample scale.

495 The relative permeability curves were affected by the saturation history under both homogeneous
496 and heterogeneous wetting conditions. The imbibition process increased the relative permeability
497 of water and decreased the relative permeability of scCO₂, compared to the drainage process.
498 Under the SWW condition, the effects of pore-scale wettability heterogeneity on the relative
499 permeability curves were not noticeable. Under heterogeneous WWW and IW conditions, the
500 variation of the scCO₂ relative permeability curve was more significant than that in the
501 homogenous wettability scenario. This is because pore-scale wettability heterogeneity enhances
502 the coalescence and snap-off behaviors of scCO₂ blobs when the system goes through the PD, IM,
503 and SD stages, thereby leading to more significant variations of scCO₂ relative permeability curves
504 at the larger scale.

505 This study demonstrated the effects of pore-scale surface wettability heterogeneity on microscopic
506 fluid distribution, macroscopic P_c - S_w relationship and relative permeability. The findings
507 advanced our understanding of the role of pore-scale wettability heterogeneity on immiscible two-
508 phase displacement in complicated 3D porous media, which has a wide range of applications in
509 many natural and engineered processes such as geological carbon storage, contaminated soil
510 remediation, flow control in micro-chips, and advanced manufacturing.

511
512

513 **Acknowledgements**

514 The authors are thankful to the financial support provided by the University Coalition for Fossil
515 Energy Research (UCFER) Program under the U.S. Department of Energy (DOE)'s National
516 Energy Technology Laboratory (NETL) through the Award Number DE-FE0026825 and
517 Subaward Number S000038-USDOE, as well as the support from NETL's Research Participation
518 Program sponsored by the U.S. DOE and administered by the Oak Ridge Institute for Science and
519 Education (ORISE). The authors also acknowledge the support of supercomputers from Virginia
520 Tech's Advanced Research Computing for the high-performance parallel computing in LB
521 multiphase flow modeling.

523 **Nomenclature**

C	Color gradient
c	Lattice speed
c_Y	Correlation function
\mathbf{e}_q	Lattice velocity vector in the q direction
f	Particle-distribution function
f_q	Particle-distribution function in the q direction
g	Mass distributions for the wetting fluid or non-wetting fluid
j_i	Fluid momentum in the i direction
k_{rg}	ScCO ₂ relative permeability
k_{rg}^o	End-point relative permeability of scCO ₂
k_{rw}	Water relative permeability
k_{rw}^o	End-point relative permeability of water
L_i	Correlation lengths in the i direction
m	Moments of particle distribution functions
m_i	Moments in the i direction
m_i^{eq}	Equilibrium moments in the i direction
M	Transform matrix
M^{-1}	Inverse of transform matrix M
n	Unit normal vector of the color gradient
n_i	Component of unit normal vector of the color gradient in the i direction
N_g	Non-wetting phase exponent in the Corey model
N_w	Wetting phase exponent in the Corey model
q	Directions in the D3Q9 lattice space
S_{grw}	Residual saturation of non-wetting phase
S_w	Wetting phase saturation
S_w^*	Normalized wetting phase saturation
S_{wir}	Irreducible saturation of wetting phase

t	Time
Δt	Time step
\mathbf{u}	Fluid velocity
w_q	Weights for the D3Q7 lattice model
\mathbf{x}	Location
x_i	Coordinate of location \mathbf{x} in the i direction
\mathbf{Y}	Field of logarithm of CA
\mathbf{y}	Location
y_i	Coordinate of location \mathbf{y} in the i direction
α	Parameter linearly related to the interfacial tension
β	Parameter that controls the width of the interface
Λ	relaxation coefficient
λ	Eigenvalue of correlation function
μ_Y	Mean of logarithm of contact angle
μ_θ	Mean of contact angle
θ	Contact angle
ρ_{nw}	Fluid density of non-wetting phase
ρ_w	Fluid density of wetting phase
σ_Y	Standard deviation of logarithm of contact angle
σ_θ	Standard deviation of contact angle
ξ_n	Independent zero-meaned Gaussian random variables with unit variance
ψ	Eigenfunction of correlation function

524

525

526

527

528

529 Reference

- 530 Akai, T., et al. (2019). Modeling Oil Recovery in Mixed-Wet Rocks: Pore-Scale Comparison Between
531 Experiment and Simulation. *Transport in Porous Media*, 127: 393-414.
- 532 Alhammadi, A. M., et al. (2017). In situ characterization of mixed-wettability in a reservoir rock at
533 subsurface conditions. *Scientific Reports*, 7.
- 534 AlRatrouf, A., et al. (2018). Wettability in complex porous materials, the mixed-wet state, and its
535 relationship to surface roughness. *Proceedings of the National Academy of Sciences of the United States*
536 *of America*, 115: 8901-8906.
- 537 Andrew, M., et al. (2014). Pore-scale contact angle measurements at reservoir conditions using X-ray
538 microtomography. *Advances in Water Resources*, 68: 24-31.
- 539 Andrew, M., et al. (2015). The Imaging of Dynamic Multiphase Fluid Flow Using Synchrotron-Based X-ray
540 Microtomography at Reservoir Conditions. *Transport in Porous Media*, 110: 1-24.
- 541 Arshadi, M., et al. (2020). Impact of mineralogy and wettability on pore-scale displacement of NAPLs in
542 heterogeneous porous media. *Journal of Contaminant Hydrology*, 230.
- 543 Bachu, S. (2002). Sequestration of CO₂ in geological media in response to climate change: road map for
544 site selection using the transform of the geological space into the CO₂ phase space. *Energy Conversion*
545 *and Management*, 43: 87-102.
- 546 Bakhshian, S. and S. A. Hosseini (2019). Pore-scale analysis of supercritical CO₂-brine immiscible
547 displacement under fractional-wettability conditions. *Advances in Water Resources*, 126: 96-107.
- 548 Bakhshian, S., et al. (2021). Physics-Driven Investigation of Wettability Effects on Two-Phase Flow in
549 Natural Porous Media: Recent Advances, New Insights, and Future Perspectives. *Transport in Porous*
550 *Media*, 140: 85-106.
- 551 Berg, S., et al. (2013). Real-time 3D imaging of Haines jumps in porous media flow. *Proceedings of the*
552 *National Academy of Sciences of the United States of America*, 110: 3755-3759.
- 553 Boek, E. S., et al. (2017). Multiphase-Flow and Reactive-Transport Validation Studies at the Pore Scale by
554 Use of Lattice Boltzmann Computer Simulations. *Spe Journal*, 22: 940-949.
- 555 Bradford, S. A. and F. J. Leij (1995). Fractional Wettability Effects on 2-Fluid and 3-Fluid Capillary
556 Pressure-Saturation Relations. *Journal of Contaminant Hydrology*, 20: 89-109.
- 557 Chang, C., et al. (2020). Impacts of Mixed-Wettability on Brine Drainage and Supercritical CO₂ Storage
558 Efficiency in a 2.5-D Heterogeneous Micromodel. *Water Resources Research*, 56.
- 559 Chen, C., et al. (2016). Optimization of Lattice Boltzmann Simulation With Graphics-Processing-Unit
560 Parallel Computing and the Application in Reservoir Characterization. *Spe Journal*, 21: 1425-1435.
- 561 Chen, C. and L. Z. Zeng (2015). Using the level set method to study the effects of heterogeneity and
562 anisotropy on hyporheic exchange. *Water Resources Research*, 51: 3617-3634.
- 563 Chen, C., et al. (2013). Continuum-scale convective mixing in geological CO₂ sequestration in anisotropic
564 and heterogeneous saline aquifers. *Advances in Water Resources*, 53: 175-187.
- 565 Chen, Z. X. and R. E. Ewing (1997). Fully discrete finite element analysis of multiphase flow in
566 groundwater hydrology. *Siam Journal on Numerical Analysis*, 34: 2228-2253.
- 567 Emami-Meybodi, H., et al. (2015). Convective dissolution of CO₂ in saline aquifers: Progress in modeling
568 and experiments. *International Journal of Greenhouse Gas Control*, 40: 238-266.
- 569 Fan, M., et al. (2019). Comprehensive study of the interactions between the critical dimensionless
570 numbers associated with multiphase flow in 3D porous media. *Fuel*, 252: 522-533.
- 571 Fan, M., et al. (2020). Influence of Clay Wettability Alteration on Relative Permeability. *Geophysical*
572 *Research Letters*, 47.
- 573 Feng, G. H., et al. (2021). Multiphase flow modeling and energy extraction performance for supercritical
574 geothermal systems. *Renewable Energy*, 173: 442-454.

575 Guo, R. C., et al. (2020). The role of the spatial heterogeneity and correlation length of surface
576 wettability on two-phase flow in a CO₂-water-rock system. *Advances in Water Resources*, 146.
577 Guo, R. C., et al. (2021). A Novel Experimental Study on Density-Driven Instability and Convective
578 Dissolution in Porous Media. *Geophysical Research Letters*, 48.
579 Hassanpouryouzband, A., et al. (2021). Offshore Geological Storage of Hydrogen: Is This Our Best Option
580 to Achieve Net-Zero? *Acs Energy Letters*, 6: 2181-2186.
581 Hewitt, G. F. (2008). Multiphase Flow in the Energy Industries. *Journal of Engineering Thermophysics*,
582 17: 12-23.
583 Hiller, T., et al. (2019). The Impact of Wetting-Heterogeneity Distribution on Capillary Pressure and
584 Macroscopic Measures of Wettability. *Spe Journal*, 24: 200-214.
585 Hu, R., et al. (2017). Wettability effects on supercritical CO₂-brine immiscible displacement during
586 drainage: Pore-scale observation and 3D simulation. *International Journal of Greenhouse Gas Control*,
587 60: 129-139.
588 Hwang, S. I., et al. (2006). Effects of fractional wettability on capillary pressure-saturation-relative
589 permeability relations of two-fluid systems. *Advances in Water Resources*, 29: 212-226.
590 Iglauer, S., et al. (2015). CO₂ wettability of seal and reservoir rocks and the implications for carbon geo-
591 sequestration. *Water Resources Research*, 51: 729-774.
592 IPCC (2018). Special Report: Global Warming of 1.5 °C. Summary for
593 Policymakers. <https://www.ipcc.ch/sr15/chapter/spm/>.
594 Landry, C. J., et al. (2014). Relative permeability of homogenous-wet and mixed-wet porous media as
595 determined by pore-scale lattice Boltzmann modeling. *Water Resources Research*, 50: 3672-3689.
596 Leclaire, S., et al. (2017). Generalized three-dimensional lattice Boltzmann color-gradient method for
597 immiscible two-phase pore-scale imbibition and drainage in porous media. *Physical Review E*, 95.
598 Li, H. N., et al. (2005). Pore-scale investigation of viscous coupling effects for two-phase flow in porous
599 media. *Physical Review E*, 72.
600 Li, Z. H., et al. (2022). Experimental investigation of non-monotonic fracture conductivity evolution in
601 energy georeservoirs. *Journal of Petroleum Science and Engineering*, 211.
602 Liu, Q., et al. (2020). Pore-scale visualization and quantitative analysis of the spontaneous imbibition
603 based on experiments and micro-CT technology in low-permeability mixed-wettability rock. *Energy*
604 *Science & Engineering*, 8: 1840-1856.
605 Masalmeh, S. K. (2002). Studying the effect of wettability heterogeneity on the capillary pressure curves
606 using the centrifuge technique. *Journal of Petroleum Science and Engineering*, 33: 29-38.
607 McClure, J. E., et al. (2021). The LBPM software package for simulating multiphase flow on digital images
608 of porous rocks. *Computational Geosciences*, 25: 871-895.
609 McClure, J. E., et al. (2010). Comparison of Cpu and Gpu Implementations of the Lattice Boltzmann
610 Method. *Proceedings of the Xviii International Conference on Computational Methods in Water*
611 *Resources (Cmwr 2010)*: 1027-1034.
612 McClure, J. E., et al. (2014). Petascale Application of a Coupled CPU-GPU Algorithm for Simulation and
613 Analysis of Multiphase Flow Solutions in Porous Medium Systems. 2014 Ieee 28th International Parallel
614 and Distributed Processing Symposium.
615 Michael, K., et al. (2010). Geological storage of CO₂ in saline aquifers -A review of the experience from
616 existing storage operations. *International Journal of Greenhouse Gas Control*, 4: 659-667.
617 Morrow, N. R. (1975). Effects of Surface-Roughness on Contact Angle with Special Reference to
618 Petroleum Recovery. *Journal of Canadian Petroleum Technology*, 14: 42-53.
619 Murison, J., et al. (2014). Wetting Heterogeneities in Porous Media Control Flow Dissipation. *Physical*
620 *Review Applied*, 2.

621 Mutailipu, M., et al. (2017). Measurements of Contact Angles for CO₂-Brine-Berea Sandstones System at
622 Reservoir Conditions. *Materials in Environmental Engineering*: 1295-1302.

623 Nemer, M. N., et al. (2020). Wettability alteration implications on pore-scale multiphase flow in porous
624 media using the lattice Boltzmann method. *Advances in Water Resources*, 146.

625 Pan, C., et al. (2004). Lattice-Boltzmann simulation of two-phase flow in porous media. *Water Resources*
626 *Research*, 40.

627 Qin, L. M., et al. (2020). Mechanistic Aspects of Polymeric Relative Permeability Modifier Adsorption
628 onto Carbonate Rocks. *Energy & Fuels*, 34: 12065-12077.

629 Rucker, M., et al. (2019). The Effect of Mixed Wettability on Pore-Scale Flow Regimes Based on a
630 Flooding Experiment in Ketton Limestone. *Geophysical Research Letters*, 46: 3225-3234.

631 Saraji, S., et al. (2013). Wettability of Supercritical Carbon Dioxide/Water/Quartz Systems: Simultaneous
632 Measurement of Contact Angle and Interfacial Tension at Reservoir Conditions. *Langmuir*, 29: 6856-
633 6866.

634 Sathaye, K. J., et al. (2014). Constraints on the magnitude and rate of CO₂ dissolution at Bravo Dome
635 natural gas field. *Proceedings of the National Academy of Sciences of the United States of America*, 111:
636 15332-15337.

637 Shi, Y. and G. H. Tang (2018). Relative permeability of two-phase flow in three-dimensional porous
638 media using the lattice Boltzmann method. *International Journal of Heat and Fluid Flow*, 73: 101-113.

639 Singh, M., et al. (2021). Coupled multiphase flow and transport simulation to model CO₂ dissolution and
640 local capillary trapping in permeability and capillary heterogeneous reservoir. *International Journal of*
641 *Greenhouse Gas Control*, 108.

642 Skauge, A., et al. (2007). Theoretical and experimental evidence of different wettability classes. *Journal*
643 *of Petroleum Science and Engineering*, 57: 321-333.

644 Tang, Y. Q., et al. (2019). Experimental Study on the Density-Driven Carbon Dioxide Convective Diffusion
645 in Formation Water at Reservoir Conditions. *Acs Omega*, 4: 11082-11092.

646 Tang, Y. Q., et al. (2019). Experimental Study on Spontaneous Imbibition of CO₂-Rich Brine in Tight Oil
647 Reservoirs. *Energy & Fuels*, 33: 7604-7613.

648 Tanino, Y. and M. J. Blunt (2013). Laboratory investigation of capillary trapping under mixed-wet
649 conditions. *Water Resources Research*, 49: 4311-4319.

650 Tokunaga, T. K., et al. (2013). Capillary pressure and saturation relations for supercritical CO₂ and brine
651 in sand: High-pressure P-c(S-w) controller/meter measurements and capillary scaling predictions. *Water*
652 *Resources Research*, 49: 4566-4579.

653 Valvatne, P. H. and M. J. Blunt (2004). Predictive pore-scale modeling of two-phase flow in mixed wet
654 media. *Water Resources Research*, 40.

655 Wang, H., et al. (2022). Deep-learning-based workflow for boundary and small target segmentation in
656 digital rock images using UNet++ and IK-EBM. *Journal of Petroleum Science and Engineering*, e110596.

657 Wei, N., et al. (2014). CO₂ flooding properties of Liujiagou sandstone: influence of sub-core scale
658 structure heterogeneity. *Greenhouse Gases-Science and Technology*, 4: 400-418.

659 Xue, W. C. and C. J. Roy (2021). Multi-GPU performance optimization of a computational fluid dynamics
660 code using OpenACC. *Concurrency and Computation-Practice & Experience*, 33.

661 Zhang, D. X. and Z. M. Lu (2004). An efficient, high-order perturbation approach for flow in random
662 porous media via Karhunen-Loeve and polynomial expansions. *Journal of Computational Physics*, 194:
663 773-794.

664 Zhao, B. Z., et al. (2016). Wettability control on multiphase flow in patterned microfluidics. *Proceedings*
665 *of the National Academy of Sciences of the United States of America*, 113: 10251-10256.

666 Zhao, J. L., et al. (2018). The Effect of Wettability Heterogeneity on Relative Permeability of Two-Phase
667 Flow in Porous Media: A Lattice Boltzmann Study. *Water Resources Research*, 54: 1295-1311.

668 Zou, S. M. and R. T. Armstrong (2019). Multiphase Flow Under Heterogeneous Wettability Conditions
669 Studied by Special Core Analysis and Pore-Scale Imaging. *Spe Journal*, 24: 1234-1247.
670